

7. Williams, A. W. S., Lightowers, E. C. & Collins, A. T. Impurity conduction in synthetic semiconducting diamond. *J. Phys. C* **3**, 1727–1735 (1970).
8. Vishnevskii, A. S., Gontar, A. G., Torishnii, V. I. & Shul'zhenko, A. A. Electrical conductivity of heavily doped p-type diamond. *Sov. Phys. Semicond.* **15**, 659–661 (1981).
9. Werner, M. *et al.* Charge transport in heavily B-doped, polycrystalline diamond films. *Appl. Phys. Lett.* **64**, 595–597 (1994).
10. Borst, T. H. & Weis, O. Boron-doped homoepitaxial diamond layers: fabrication, characterization and electronic applications. *Phys. Status Solidi A* **154**, 423–444 (1996).
11. Zhang, R. J., Lee, S. T. & Lam, Y. W. Characterization of heavily boron-doped diamond films. *Diamond Relat. Mater.* **5**, 1288–1294 (1996).
12. Eremets, M. I., Struzhkin, V. V., Mao, H.-K. & Hemley, R. J. Superconductivity in boron. *Science* **293**, 272–274 (2001).
13. Werthamer, N. R., Helfand, E. & Hohenberg, P. C. Temperature and purity dependence of the superconducting critical field H_{c2} , III. Electron spin and spin-orbit effects. *Phys. Rev.* **147**, 295–302 (1966).
14. McMillan, W. L. Transition temperature of strongly coupled superconductors. *Phys. Rev.* **167**, 331–344 (1968).
15. Gurevich, V. L., Larkin, A. I. & Firsov, Yu. A. On the possibility of superconductivity in semiconductors. *Sov. Phys. Solid State* **4**, 131–135 (1962).
16. Cohen, M. L. Superconductivity in many-valley semiconductors and in semimetals. *Phys. Rev.* **134**, A511–A521 (1964).
17. Cohen, M. L. in *Superconductivity* (ed. Parks, R. D.) Vol. 1, 615–644 (Marcel Dekker, New York, 1969).
18. Kohmoto, M. & Takada, Y. Superconductivity from an insulator. *J. Phys. Soc. Jpn* **59**, 1541–1544 (1990).
19. Nozières, P. & Pistoiesi, F. From semiconductors to superconductors: a simple model for pseudogaps. *Eur. Phys. J. B* **10**, 649–662 (1999).
20. Hulm, J. K., Ashkin, M., Deis, D. W. & Jones, C. K. in *Progress in Low Temperature Physics* (ed. Gorter, C. J.) Vol. VI, 205–242 (North-Holland, Amsterdam, 1970).
21. Kawaji, H., Horie, H., Yamanaka, S. & Ishikawa, M. Superconductivity in the silicon clathrate compound $(\text{Na,Ba})_x\text{Si}_{146}$. *Phys. Rev. Lett.* **74**, 1427–1429 (1995).
22. Grosche, F. M. *et al.* Superconductivity in the filled cage compounds $\text{Ba}_6\text{Ge}_{25}$ and $\text{Ba}_4\text{Na}_2\text{Ge}_{25}$. *Phys. Rev. Lett.* **87**, 247003 (2001).
23. Khvostantsev, L. G., Vereshchagin, L. F. & Novikov, A. P. Device of toroid type for high pressure generation. *High Temp. High Press.* **9**, 637–639 (1977).
24. Voronov, O. A. & Rakhmanina, A. V. Parameter of the cubic cell of diamond doped with boron. *Inorg. Mater.* **29**, 707–710 (1993).
25. Brunet, F., Deneuve, A., Germe, P., Pernet, M. & Gheeraert, E. Variation of the cell parameter of polycrystalline boron doped diamond films. *J. Appl. Phys.* **81**, 1120–1125 (1997).
26. Bean, C. P. Magnetization of hard superconductors. *Phys. Rev. Lett.* **8**, 250–253 (1962).

Acknowledgements We thank D. Wayne for mass spectrometry measurements of the B content of our samples, A. Prez for SEM images and S. Gierlotka for help in sample analysis. This work was supported by the Russian Foundation for Basic Research and by the Strongly Correlated Electrons Program of the Department of Physical Sciences, Russian Academy of Sciences. Work at Los Alamos was performed under the auspices of the US DOE.

Authors' contributions Boron-doped diamond samples were synthesized by E.A.E., and their physical properties measured by V.A.S., E.D.B., N.N.M., N.J.C., J.D.T. and S.M.S.

Competing interests statement The authors declare that they have no competing financial interests.

Correspondence and requests for materials should be addressed to V.A.S. (sidorov@hppi.troitsk.ru)

.....

Intermediate-depth earthquake faulting by dehydration embrittlement with negative volume change

Haemyeong Jung¹, Harry W. Green II^{1,2} & Larissa F. Dobrzhinetskaya²

¹Institute of Geophysics and Planetary Physics, ²Department of Earth Sciences, University of California, Riverside, California 92521, USA

Earthquakes are observed to occur in subduction zones to depths of approximately 680 km, even though unassisted brittle failure is inhibited at depths greater than about 50 km, owing to the high pressures and temperatures^{1–3}. It is thought that such earthquakes (particularly those at intermediate depths of 50–300 km)

may instead be triggered by embrittlement accompanying dehydration of hydrous minerals, principally serpentine^{1–3}. A problem with failure by serpentine dehydration is that the volume change accompanying dehydration becomes negative at pressures of 2–4 GPa (60–120 km depth), above which brittle fracture mechanics predicts that the instability should be quenched^{4,5}. Here we show that dehydration of antigorite serpentine under stress results in faults delineated by ultrafine-grained solid reaction products formed during dehydration. This phenomenon was observed under all conditions tested (pressures of 1–6 GPa; temperatures of 650–820 °C), independent of the sign of the volume change of reaction. Although this result contradicts expectations from fracture mechanics, it can be explained by separation of fluid from solid residue before and during faulting, a hypothesis supported by our observations. These observations confirm that dehydration embrittlement is a viable mechanism for nucleating earthquakes independent of depth, as long as there are hydrous minerals breaking down under a differential stress.

A popular hypothesis for overcoming brittle fracture inhibition, especially for earthquakes at intermediate depths (<300 km), is assistance of brittle fracture by generation of a free fluid as a result of dehydration of serpentine or other hydrous minerals^{1–3,6–11}. The phenomenon of dehydration embrittlement was discovered almost 40 years ago¹ but has been studied only sporadically since that time^{4–8}. In particular, this phenomenon has not been addressed by controlled deformation experiments at pressures greater than 700 MPa, equivalent to only ~20 km depth in Earth. Studies of acoustic emission at elevated pressures^{5,8}, however, have implications for deeper earthquakes. The latter studies, although lacking control of differential stress, strain, or strain rate, recorded acoustic emissions at much higher pressures and inferred that faulting had occurred.

The fracture mechanics explanation of how dehydration embrittlement can enable brittle shear failure at elevated pressure is based upon production of a pore pressure as a consequence of a positive volume change, ΔV , of the dehydration reaction and consequent decrease in the effective pressure on existing or potential planes of weakness. Thus, as conventionally understood, the theory predicts that if the ΔV of the reaction were to become negative, failure would become more difficult and the shearing instability would vanish^{4,5}. Because hydrous fluid is much more compressible than solid silicates, the total ΔV of dehydration of the common hydrous phases of primary interest (for example, serpentine and chlorite) is progressively reduced as pressure increases and becomes negative at pressures of 2–4 GPa, equivalent to pressures of 60–120 km in Earth. One consequence of this prediction is that earthquakes should not be possible by dehydration embrittlement at greater depths⁵. However, dehydration embrittlement is the only earthquake nucleation mechanism known to be viable for depths less than 300 km (ref. 2). Thus, it is important to determine whether this mechanism can function under conditions where ΔV is negative.

We report here the results of deformation experiments at pressures of 1–6 GPa and temperatures of 550–820 °C using an antigorite serpentine from Val Malenco, Italy, for which the phase diagram has been measured¹². Figure 1a shows the experimental conditions investigated; the slope of the high-temperature limit of antigorite stability (Fig. 1a) is negative above ~2.2 GPa, reflecting negative ΔV of reaction above that pressure.

Figure 1b–f shows microstructures of the starting material and results of annealing without deformation outside antigorite stability. The layering, strong foliation and proportions of antigorite and relict olivine shown are typical of our starting material. Figure 1f shows breakdown of antigorite along boundaries with relict olivine and healed cracks of several orientations outlined by fluid inclusions; such inclusion trails are rare in the starting material,

hence clearly were produced during the experiment. Similar healed cracks are abundant and strongly oriented in deformed specimens (see below).

One specimen was deformed within the stability field of antigorite (triangle in Fig. 1a). This specimen was extremely strong ($\sigma_1 - \sigma_3 = 1.5$ GPa) and failed by conventional brittle fracture; no sign of dehydration products was found within the specimen after deformation (σ_1 is maximum compressive stress; σ_3 is minimum compressive stress). All other specimens deformed in the Griggs apparatus failed at significantly lower stresses (for example, 0.8–0.9 GPa at $\sigma_3 = 1$ GPa), exhibiting multiple faults. Except in complicated multi-fault regions, faults are aligned $\sim 25\text{--}40^\circ$ to the maximum applied stress, σ_1 . Figure 2a–c shows fault displacements demonstrated by offsets of specimen surfaces, regions of relict olivine, and across films of Ni incorporated as described in Methods. Figure 2d–f shows details of the breakdown of antigorite adjacent to relict olivine where progression of the reaction can be

seen much more clearly than in the antigorite matrix. Many grain boundaries are open and show cusps along them, reflecting dissolution of olivine by the fluid released during antigorite decomposition. Open Mode I cracks parallel to σ_1 (top–bottom in photographs) are abundant, as are healed cracks outlined by fluid inclusion trails. Open cracks display cusps with smaller cracks, commonly healed, emanating from them.

Faults all contain ultrafine-grained aggregates (≤ 300 nm) of solid dehydration products that consist primarily of olivine, as shown by energy-dispersive spectroscopy (EDS) analysis and bright contrast. Although the ΔV of reaction is strongly positive at 1.0 GPa, moderately positive at 1.7 GPa and distinctly negative at 3.3 and 6 GPa, all specimens showed the same ‘wispy’ pattern of solid reaction products preserved within and along the faults.

Figure 3a (pressure $P = 1.7$ GPa) shows a fault that branches near the centre of the image. The branch to the right ends near the top of the image (arrowheads), with the wispy dehydration products changing orientation to approximately normal to macroscopic σ_1 (top–bottom), defining surfaces akin to stylolites¹³ or anticracks¹⁴ (surfaces across which contraction has occurred and volume has been lost). The right-lateral shear on this fault system is such that the triangular region near the branch (arrow) is in compression and displays a high density of dehydration product lenses. It is well known that faults at Earth’s surface commonly show *en echelon* fault segments, with ‘pull-aparts’ between them¹⁵. The inset of Fig. 3a shows an analogous feature that is very common in our experiments in which, rather than a ‘pull-apart’, a ‘push-together’ is formed between *en echelon* fault segments arranged such that the region between their overlapping tips has experienced contraction rather than extension. The region of the ‘push-together’ has an abundance of dehydration products defining anticrack lenses that have accommodated shortening in response to the enhanced compression. Figure 3b ($P = 6$ GPa) shows a series of such ‘push-togethers’ (also shown diagrammatically in Fig. 3c for clarity), again showing

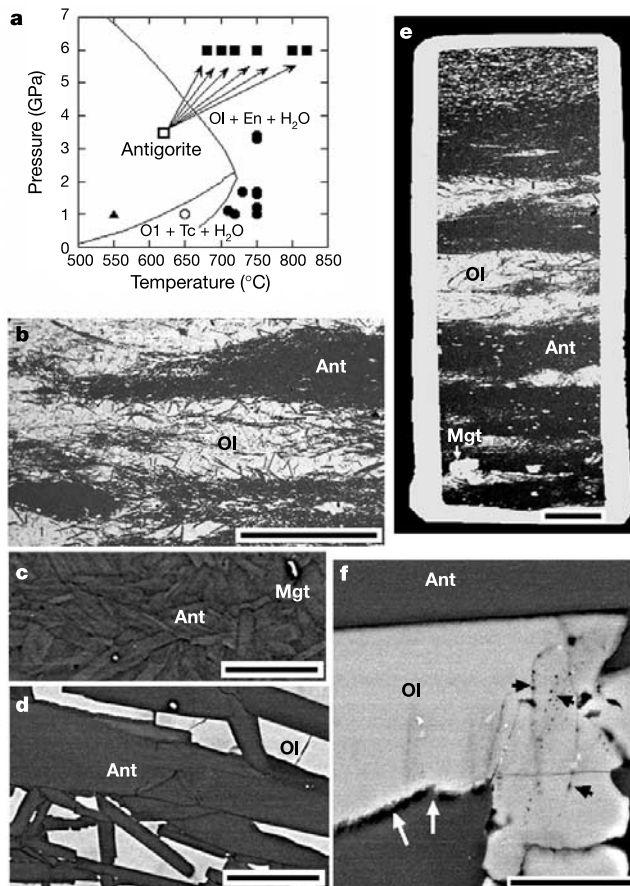


Figure 1 Experimental conditions and starting material for deformation experiments. **a**, Phase diagram for antigorite¹² and experimental conditions. Ol, olivine; En, enstatite; Tc, talc. Open symbols, hydrostatic experiments. Filled circles, deformation experiments in modified Griggs apparatus (strain rate $2 \times 10^{-4} \text{ s}^{-1}$). Filled squares, experiments in Walker-type multianvil apparatus; arrows indicate P/T paths during rapid pumping, yielding strain rates approximating those in the Griggs apparatus. All deformation experiments displayed faults and evidence of antigorite breakdown except the experiment within antigorite stability (filled triangle). **b–d**, Microstructure of starting material: antigorite (Ant), relict olivine (Ol), and minor magnetite (Mgt). **e, f**, Specimen pressurized to 1.0 GPa and annealed for 1 h at 650 °C (open circle in **a**). Pt capsule (white) and specimen are undeformed. **f**, Minor antigorite breakdown (arrows) yields fluid inclusion trails (arrowheads) on healed cracks of several orientations. Scale bars: 1 mm (**b, e**); 10 μm (**c, d, f**).

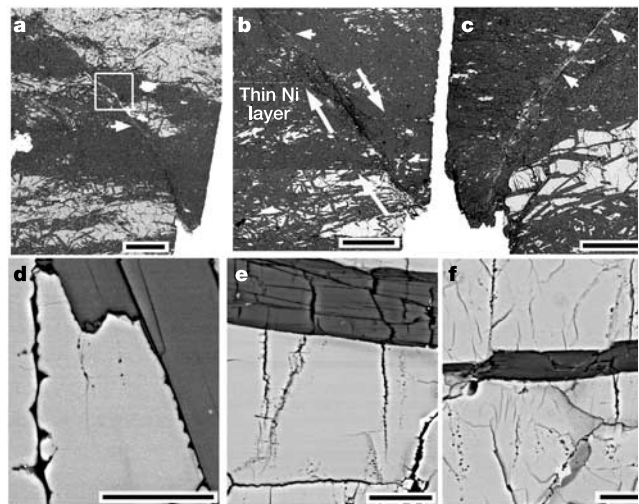


Figure 2 Microstructures of faulted specimens. **a**, Fault offsetting layers richer and poorer in relict olivine (1.7 GPa, 750 °C; $\Delta V > 0$); square shows location of Fig. 3a. **b**, Fault displacing Ni films (arrows) (1.0 GPa, 720 °C; $\Delta V > 0$). **c**, Similar to **a** but 3.3 GPa, 750 °C; $\Delta V < 0$. Dehydration products along faults in **a–c** indicated by arrowheads. **d–f**, Open Mode I cracks (σ_1 is top–bottom in image) with multiple cusps showing dissolution of olivine and fluid inclusion trails outlining healed Mode I cracks. Minor irregular cracking during decompression after experiment also visible. **d**, 1.7 GPa, 750 °C; $\Delta V > 0$. **e**, 1.7 GPa, 730 °C; $\Delta V > 0$. **f**, 6 GPa, 750 °C; $\Delta V < 0$. Scale bars: 200 μm (**a–c**); 10 μm (**d**); 20 μm (**e, f**).

that the dehydration products decorate surfaces of maximum compression. Figure 3d ($P = 1.0$ GPa) shows another fault trace that displays the same features as described in Fig. 3a–c. In this case, branching of the fault zone is seen at the top left corner of the image, with compression (anticrack) lenses in the squeezed wedge at the branch point (star), and several ‘push-togethers’, marked by arrowheads, are strung out along the fault trace. These panels also show that the extent of reaction outside fault zones is distinctly less than within them, suggesting that the fault zones have self-organized and propagated from points where the reaction initiated.

In summary, dehydration of antigorite under stress at pressures of 1–6 GPa leads to faulting under all conditions tested. Moreover, we document the presence of abundant healed cracks marked by fluid inclusion trails on surfaces of least normal stress (parallel to σ_1) and lenses of solid reaction products located preferentially on surfaces of highest normal stress (normal to σ_1), showing that the fluid and solid products of antigorite breakdown become separated during faulting. Thus, free fluid of density lower than antigorite was

available at all pressures to generate abundant Mode I cracks and lead to shear failure². Faulting apparently in conflict with fracture mechanics theory is explained by separation of fluid (lower density than antigorite—positive ΔV) and solid reaction products (higher density than antigorite—negative ΔV) during deformation. Each component is concentrated on appropriate surfaces to help accommodate the local strain field.

Returning to consideration of Fig. 3, we note that during growth of a fault (or growth of a slip patch on an existing fault), at any point in that growth the stress distribution resulting from its displacement field is as sketched in Fig. 4a. As the slipping patch grows, there is continuing renewal of such stressed regions, with the compressive zones sketched in Fig. 4b, c. Thus, such a fault patch evolving in a system in which an on-going reaction produces a fluid/solid slurry is ideally situated to focus the reaction in local regions of enhanced compression, leading to concentration of the denser solids on planes of high normal stress as microanticracks and expelling the less-dense fluid into the fault zone where it reduces friction and lubricates the fault surface. The result of such a scenario would be

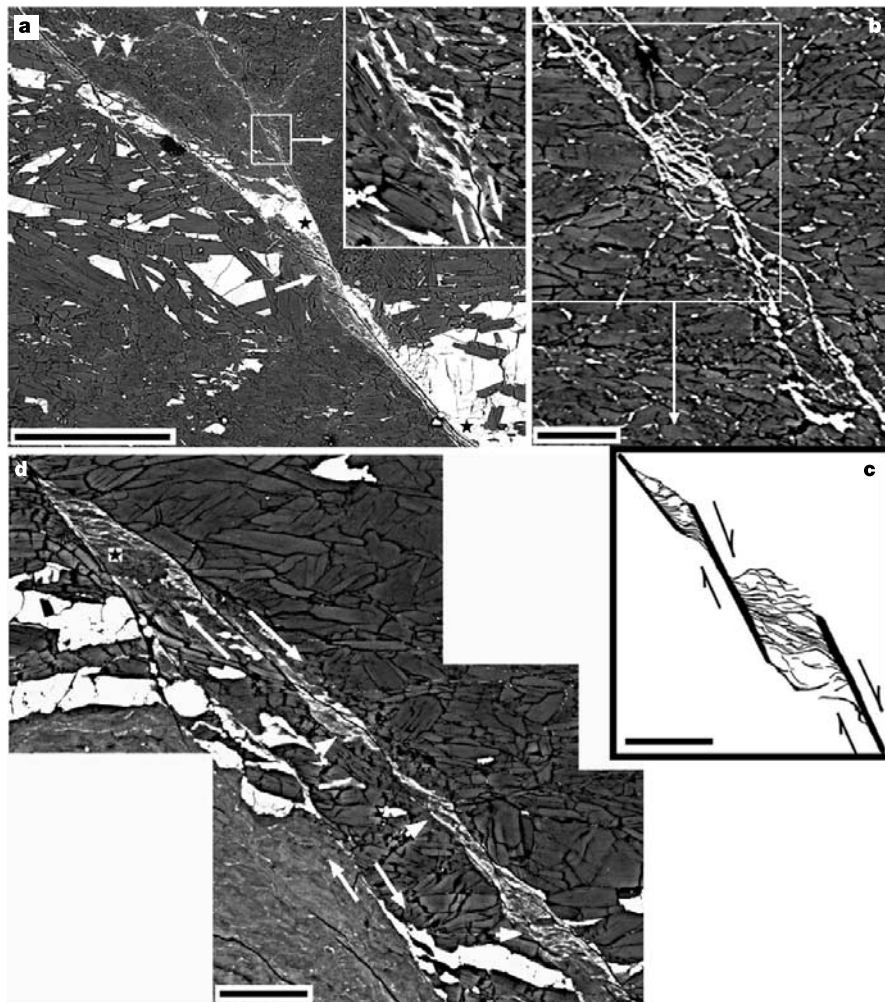


Figure 3 Fault microstructures. **a**, Detail of Fig. 2a. Fault shows minor branch that dies out near top of image, outlined by ‘wisps’ of solid reaction products at high angles to σ_1 (arrowheads). Convergence near branch point (arrow) is under compression and exhibits a concentration of ‘wisps’. Stars show fault displacement of a severed magnetite blob. Inset shows multiple anticrack ‘wisps’ in ‘push-together’ between overlapping ends of *en echelon* microfaults (1.7 GPa; $\Delta V > 0$). **b**, Topologically identical series of ‘push-togethers’ between *en echelon* fault segments at 6 GPa ($\Delta V < 0$). **c**, Schematic

drawing of part of fault zone in **b**; heavier lines are fault segments and lighter lines are traces of the solid reaction products. **d**, Similar microstructures at 1.0 GPa ($\Delta V > 0$); ‘push-togethers’ (arrowheads) and a converging zone (star) are again decorated by solid reaction products oriented normal to the orientation of the local σ_1 (top–bottom). Open cracks in the fault zones are decompression features. Scale bars: 100 μm (**a**); 20 μm (**b–d**).

microstructures like those shown in Fig. 3. Remarkably similar structures (except showing 'pull-aparts') have been shown in small natural faults^{13,14} (Fig. 4d), and 'push-togethers' have been seen previously between the tips of *en echelon* faults produced by transformation-induced faulting in Mg₂GeO₄ during the olivine-spinel transformation¹⁶.

These results show that dehydration embrittlement as a mechanism for initiation of earthquakes is not restricted to conditions where the total volume change of reaction is positive ($\Delta V > 0$). It is clear that in our experiments the self-organization of the shear failure process includes separation of fluid from solid reaction products, thereby extending the potential operation of pore-pressure-induced faulting to all conditions where the density of the fluid

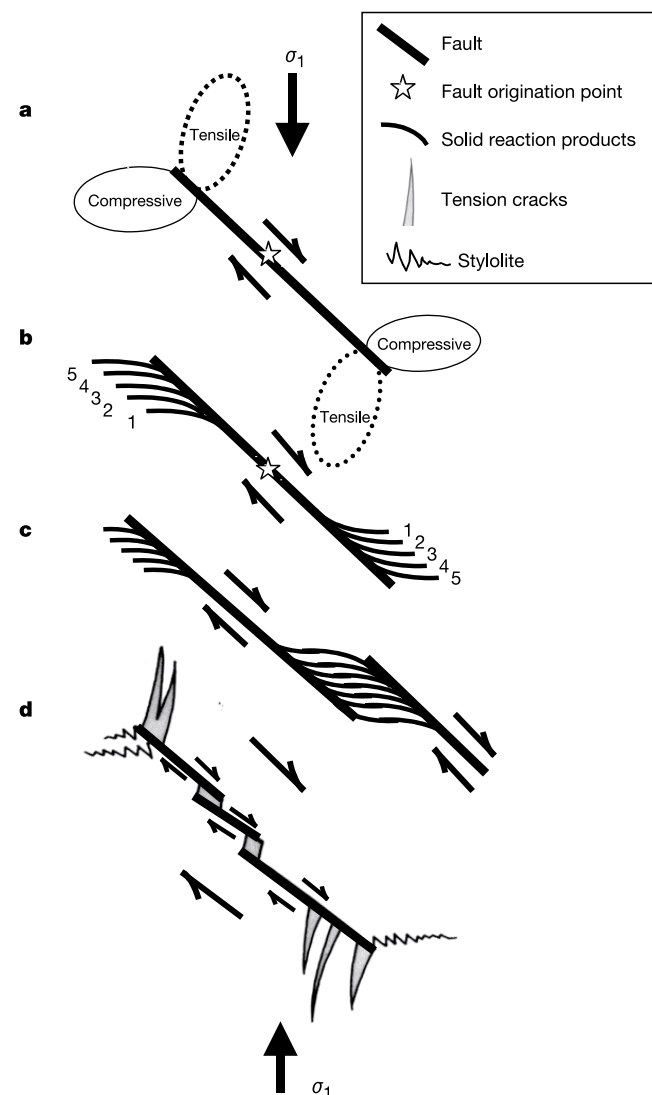


Figure 4 Hypothetical evolution of observed fault microstructure. **a**, Stress distribution at tips of growing fault. **b**, Potential microstructure developed along a newly formed microfault in which solid components ($\Delta V < 0$) are preserved periodically (sequential positions marked 1–5) and fluid components ($\Delta V > 0$) are not preserved (perhaps pumped into the evolving fault zone). Note that solid reaction products are oriented normal to local σ_1 . **c**, *En echelon* array of microfaults with characteristics illustrated in **b**. **d**, Sketched natural fault in limestone (modified after Fig. 3 of ref. 13) showing both tension cracks (filled with calcite) and compression stylolites. Note that *en echelon* stepping is the reverse sense from our high-pressure faults, yielding 'pull-aparts' (also filled with calcite).

generated is less than that of the solid phase from which the fluid is derived. That would surely include all conditions obtaining in Earth's upper mantle except perhaps at simultaneously high pressures and temperatures where solubility of rock components in fluid becomes very high¹⁷, potentially yielding melts more dense than the rock from which they are derived¹⁸.

Arguments that dehydration embrittlement can explain all intermediate-depth earthquakes (and perhaps deep earthquakes as well) have become common in recent years, both from the standpoint of seismology¹⁹ and petrology^{9,11,20}. Our results are supportive of this concept if the requisite dehydration reaction is occurring. On the other hand, serious questions have been raised about the ability of this mechanism to explain the lower plane of earthquakes in double seismic zones because the presence of hydrous phases would be required to depths of 40 km or more immediately beneath oceanic trenches. One potential resolution of this quandary is that deep penetration of H₂O perhaps occurs on major faults of the oceanic lithosphere, leading to hydrous alteration along them to the required depths^{19,21}. However, a recent study of the Vanuatu subduction zone²² shows that new faults are generated during subduction, an observation that would require more extensive hydrous alteration than solely along pre-existing faults. Reference 20 suggests up dip flow of fluid along the dehydration reaction boundary, a mechanism that might be plausible, but to produce earthquakes directly below the trench, the fluid would have to continue to flow beyond the point where any subduction-related hydration could have reached that depth. The growing sophistication of seismic studies of subduction zones holds great promise for measuring the distribution of hydrous phases²³.

Lastly, recent laboratory experiments have demonstrated that generation of less than 1% fluid, if appropriately distributed, can be sufficient to enable faulting²⁴. As a consequence, it is possible that dehydration of even minor hydrous phases such as clinohumite in peridotite or phengite in eclogite could trigger earthquakes as deep as 400 km (ref. 25). Moreover, discovery of seismic reflectors that move²⁶ in fault zones of the continental crust clearly demonstrates fluid saturation in such fault zones. Therefore, hydrous alteration of crustal minerals must be widespread at seismogenic depths in continents, and dehydration of clays or other hydrous minerals just before (or in the early stages of) crustal faulting could also contribute significantly to initiation or enhancement of shallow earthquakes. □

Methods

Several studies of antigorite stability have yielded varying results that are attributed to variations in structure and Al content²⁷. For the results presented here, that uncertainty is not a problem for two reasons: (1) our results are dependent only on the running of the dehydration reaction, not the specific location of phase boundaries; (2) our starting material is the same as that used in ref. 12, hence we know the positions of the phase boundaries (Fig. 1a).

Experiments at pressures ≤ 3.4 GPa were conducted in a modified Griggs apparatus with sample assemblies illustrated previously^{24,28}. Samples were right circular cylinders, 3.1 mm diameter and 8.4 mm long, encapsulated in Pt with oxygen fugacity buffered at Ni/NiO. CsCl, an extremely weak solid, was used as pressure medium to minimize friction of the apparatus. In order to document small fault offsets, some experiments were composed of stacks of 20–25 disks with Ni evaporated on one surface of each disk. Pressure was increased to 40 MPa at room temperature with further pressurization at 300 °C. The temperature was then increased to the desired temperature, annealed for 0–60 min, and deformed at a strain rate of $2 \times 10^{-4} \text{ s}^{-1}$. Samples were quenched to room temperature in seconds following deformation. Each experiment contained thermocouples at both the top and bottom of the specimen; the temperature difference between them was generally less than $\sim 10^\circ\text{C}$. Experiments at pressures of 3.5–6 GPa were conducted using a Walker-type multianvil device with a single thermocouple in the centre of the specimen. The multianvil is designed to generate hydrostatic stresses. However, with Al₂O₃ pistons at the ends of fully-dense specimens, rapid pumping can generate the necessary differential stress to produce faulting²⁹. Therefore, samples were initially pressurized cold to 3.5 GPa and temperature raised to 620 °C followed by rapid simultaneous increase in pressure and temperature along the arrows shown in Fig. 1a over 5–9 min. No measurement of stress is possible in specimens deformed in the multianvil but, as shown in Figs 2 and 3, microstructures of faulted specimens were indistinguishable from those in the Griggs rig. Some specimens were made up of stacked disks of starting material on which Ni

films were evaporated on the disk surfaces, yielding well-defined internal markers of fault offsets. All deformed specimens were observed by optical and scanning electron microscopy (SEM); all half-tone figures are back-scattered electron images taken at 20 kV acceleration voltage with a Philips XL-30 SEM with a field emission gun.

Received 17 November 2003; accepted 17 February 2004; doi:10.1038/nature02412.

- Raleigh, C. B. & Paterson, M. S. Experimental deformation of serpentinite and its tectonic implications. *J. Geophys. Res.* **70**, 3965–3985 (1965).
- Green, H. W. & Houston, H. The mechanics of deep earthquakes. *Annu. Rev. Earth Planet. Sci.* **23**, 169–213 (1995).
- Kirby, S. Intralab earthquakes and phase changes in subducting lithosphere. *Rev. Geophys.* **33**(suppl.), 287–297 (1995).
- Wong, T.-F., Ko, S. C. & Olgaard, D. L. Generation and maintenance of pore pressure excess in a dehydrating system, 2. Theoretical analysis. *J. Geophys. Res.* **102**, 841–852 (1997).
- Dobson, D. P., Meredith, P. G. & Boon, S. A. Simulation of subduction zone seismicity by dehydration of serpentinite. *Science* **298**, 1407–1410 (2002).
- Murrell, S. A. F. & Ismail, I. A. H. The effect of decomposition of hydrous minerals on the mechanical properties of rocks at high pressures and temperatures. *Tectonophysics* **31**, 207–258 (1976).
- Rutter, E. H. & Brodie, K. H. Experimental “syntectonic” dehydration of serpentinite under conditions of controlled pore water pressure. *J. Geophys. Res.* **93**, 4907–4932 (1988).
- Meade, C. & Jeanloz, R. Deep-focus earthquakes and recycling of water into the earth’s mantle. *Science* **252**, 68–72 (1991).
- Peacock, S. Are the lower planes of double seismic zones caused by serpentinite dehydration in subducting oceanic mantle? *Geology* **29**, 299–302 (2001).
- Seno, T., Zhao, D., Kobayashi, Y. & Nakamura, M. Dehydration of serpentinized slab mantle: seismic evidence from southwest Japan. *Earth Planets Space* **53**, 861–871 (2001).
- Omori, S., Kamiya, S., Maruyama, S. & Zhao, D. Morphology of the intraslab seismic zone and devolatilization phase equilibria of the subducting slab peridotite. *Bull. Earthq. Res. Inst. Univ. Tokyo* **76**, 455–478 (2002).
- Ulmer, P. & Trommsdorff, V. Serpentine stability to mantle depths and subduction related magmatism. *Science* **268**, 858–861 (1995).
- Rispoli, R. Stress fields about strike-slip faults inferred from stylolites and tension gashes. *Tectonophysics* **75**, T29–T36 (1981).
- Fletcher, R. C. & Pollard, D. D. Anticrack model for pressure solution surfaces. *Geology* **9**, 419–424 (1981).
- Aydin, A. & Nur, A. Evolution of pull-apart basins and their scale independence. *Tectonics* **1**, 91–105 (1982).
- Burnley, P. C. *The Effect of Nonhydrostatic Stress on the Olivine-spinel Transformation in Mg₂GeO₄*. Thesis, Univ. California, Davis (1990).
- Bureau, H. & Kepler, H. Complete miscibility between silicate melts and hydrous fluids in the upper mantle: experimental evidence and geochemical implications. *Earth Planet. Sci. Lett.* **165**, 187–196 (1999).
- Agee, C. B. & Walker, D. Static compression and olivine flotation in ultrabasic silicate liquid. *J. Geophys. Res.* **93**, 3437–3449 (1988).
- Silver, P. G. *et al.* Rupture characteristics of the deep Bolivian earthquake of 1994 and the mechanism of deep-focus earthquakes. *Science* **268**, 69–73 (1995).
- Hacker, B. R., Peacock, S. M., Abers, G. A. & Holloway, S. D. Subduction factory – 2. Are intermediate-depth earthquakes in subducting slabs linked to metamorphic dehydration reaction? *J. Geophys. Res.* **108**, doi:10.1029/2001JB001129 (2003).
- Jiao, W., Silver, P. G., Fei, Y. & Prewitt, C. T. Do intermediate- and deep focus earthquakes occur on preexisting weak zones? An examination of the Tonga subduction zone. *J. Geophys. Res.* **105**, 28125–28138 (2000).
- Christova, C. & Scholz, C. H. Stresses in the Vanuatu subducting slab: A test of two hypotheses. *Geophys. Res. Lett.* **30**, doi:10.1029/2003GL017701 (2003).
- Zhao, D., Mishra, O. P. & Sanda, R. Influence of fluids and magma on earthquakes: seismological evidence. *Phys. Earth. Planet. Inter.* **132**, 249–267 (2002).
- Zhang, J., Green, H. W. II, Bozhilov, K. N. & Jin, Z.-M. Faulting induced by precipitation of water at grain boundaries in hot subducting oceanic crust. *Nature* (in the press).
- Stalder, R. & Ulmer, P. Phase relations of a serpentinite composition between 5 and 14 GPa: significance of clinohumite and phase E as water carriers into the transition zone. *Contrib. Mineral. Petrol.* **140**, 670–679 (2001).
- Niu, F., Silver, P. G., Nadeau, R. M. & McEvilly, T. V. Migration of seismic scatterers associated with the 1993 Parkfield aseismic transient event. *Nature* **426**, 544–548 (2003).
- Bromiley, G. D. & Pawley, A. R. The stability of antigorite in the systems MgO-SiO₂-H₂O (MSH) and MgO-Al₂O₃-SiO₂-H₂O (MASH): The effects of Al³⁺ substitution on high-pressure stability. *Am. Mineral.* **88**, 99–108 (2003).
- Green, H. W. II & Borch, R. S. A new molten salt cell for precision stress measurement at high pressure. *Eur. J. Mineral.* **1**, 213–219 (1989).
- Green, H. W., Young, T. E., Walker, D. & Scholz, C. H. Anticrack-associated faulting at very high-pressure in natural olivine. *Nature* **348**, 720–722 (1990).

Acknowledgements We thank V. Trommsdorff for sample material corresponding to that used in ref. 12; J. Zhang for discussions; K. Bozhilov for assistance with microscopy and photography; and F. Forgit for specimen assembly preparation and laboratory assistance. This work was supported by the US National Science Foundation.

Competing interests statement The authors declare that they have no competing financial interests.

Correspondence and requests for materials should be addressed to H.W.G. (hgreen@mail.ucr.edu).

The decline and fate of an iron-induced subarctic phytoplankton bloom

Philip W. Boyd¹, Cliff S. Law², C.S. Wong³, Yukihiko Nojiri⁴, Atsushi Tsuda⁵, Maurice Levasseur⁶, Shigenobu Takeda⁷, Richard Rivkin⁸, Paul J. Harrison^{9,10}, Robert Strzepek¹¹, Jim Gower³, R. Mike McKay¹², Edward Abraham², Mike Arychuk³, Janet Barwell-Clarke³, William Crawford³, David Crawford³, Michelle Hale⁸, Koh Harada¹³, Keith Johnson³, Hiroshi Kiyosawa¹⁴, Isao Kudo¹⁵, Adrian Marchetti¹⁶, William Miller¹⁷, Joe Needoba⁹, Jun Nishioka¹⁸, Hiroshi Ogawa¹⁹, John Page³, Marie Robert³, Hiroaki Saito²⁰, Akash Sastri²¹, Nelson Sherry⁹, Tim Soutar³, Nes Sutherland³, Yosuke Taira⁵, Frank Whitney³, Shau-King Emmy Wong³ & Takeshi Yoshimura¹⁸

- ¹NIWA Centre for Chemical and Physical Oceanography, Department of Chemistry, University of Otago, PO Box 56, Dunedin, 9003, New Zealand
²National Institute of Water and Atmospheric Research, 301 Evans Bay Parade, Greta Point, PO Box 14-901, Kilbirnie, Wellington, New Zealand
³Fisheries and Oceans Canada, Institute of Ocean Sciences, PO Box 6000, Sidney, British Columbia, V8L 4B2 Canada
⁴National Institute for Environmental Studies, Tsukuba, Ibaraki 305-8506, Japan
⁵Ocean Research Institute, University of Tokyo, Nakano, Tokyo 164-8639, Japan
⁶Department of Biology, University of Laval, Quebec, G1K 7P4, Canada
⁷Department of Aquatic Bioscience, University of Tokyo, Bunkyo, Tokyo 113-8657, Japan
⁸Ocean Sciences Centre, Memorial University of Newfoundland, St John’s, Newfoundland, A1C 5S7, Canada
⁹Earth and Ocean Sciences, University of British Columbia, 6270 University Blvd, Vancouver, British Columbia, V6T 1Z4, Canada
¹⁰Hong Kong University of Science and Technology, Clear Water Bay, Hong Kong
¹¹Department of Chemistry, University of Otago, PO Box 56, Dunedin, 9003, New Zealand
¹²Department of Biological Sciences, Bowling Green State University, Bowling Green, Ohio 43403, USA
¹³National Institute of Advanced Industrial Science and Technology, 1-3-1, Kasumigaseki, Chiyoda-ku, Tokyo 100-8921, Japan
¹⁴Marine Biological Research Institute of Japan, Shinagawa, Tokyo 142-0042, Japan
¹⁵Graduate School of Fisheries Science, Hokkaido University, Hakodate, Hokkaido 041-8611, Japan
¹⁶Department of Botany, University of British Columbia, 6270 University Blvd, Vancouver, British Columbia, V6T 1Z4, Canada
¹⁷Dalhousie University, Department of Oceanography, Halifax, Nova Scotia, B3H 4J1 Canada
¹⁸Central Research Institute of Electric Power Industry, Abiko, Chiba 270-1194, Japan
¹⁹Marine Biogeochemistry Laboratory, Ocean Research Institute, The University of Tokyo 1-15-1, Minamidai, Nakano, Tokyo 164-8639, Japan
²⁰Tohoku National Fisheries Research Institute, Shiogama, Miyagi 985-0001, Japan
²¹School of Earth and Ocean Sciences, University of Victoria, Victoria, British Columbia, V8W 3N5, Canada

Iron supply has a key role in stimulating phytoplankton blooms in high-nitrate low-chlorophyll oceanic waters^{1–5}. However, the fate of the carbon fixed by these blooms, and how efficiently it is exported into the ocean’s interior, remains largely unknown^{1–5}. Here we report on the decline and fate of an iron-stimulated diatom bloom in the Gulf of Alaska. The bloom terminated on day 18, following the depletion of iron and then silicic acid, after which mixed-layer particulate organic carbon (POC) concentrations declined over six days. Increased particulate silica export via sinking diatoms was recorded in sediment traps at depths between 50 and 125 m from day 21, yet increased POC export was not evident until day 24. Only a small proportion of the